

# Hyperspectral image reconstruction for spectral camera based on ghost imaging via sparsity constraints using V-DUnet

Ziyan Chen, Zhentao Liu, Chenyu Hu, Heng Wu, Jianrong Wu, Jinda Lin, Zhishen Tong, Hong Yu, and Shensheng Han

**Abstract**—Spectral camera based on ghost imaging via sparsity constraints (GISC spectral camera) obtains three-dimensional (3D) hyperspectral information with two-dimensional (2D) compressive measurements in a single shot, which has attracted much attention in recent years. However, its imaging quality and real-time performance of reconstruction still need to be further improved. Recently, deep learning has shown great potential in improving the reconstruction quality and reconstruction speed for computational imaging. When applying deep learning into GISC spectral camera, there are several challenges need to be solved: 1) how to deal with the large amount of 3D hyperspectral data, 2) how to reduce the influence caused by the uncertainty of the random reference measurements, 3) how to improve the reconstructed image quality as far as possible. In this paper, we present an end-to-end V-DUnet for the reconstruction of 3D hyperspectral data in GISC spectral camera. To reduce the influence caused by the uncertainty of the measurement matrix and enhance the reconstructed image quality, both differential ghost imaging results and the detected measurements are sent into the network's inputs. Compared with compressive sensing algorithm, such as PICHCS and TwIST, it not only significantly improves the imaging quality with high noise immunity, but also speeds up the reconstruction time by more than two orders of magnitude.

**Index Terms**—Convolution neural network, Deep learning, Ghost imaging, Hyperspectral image reconstruction.

## I. INTRODUCTION

HOST imaging (GI) obtains the image information through intensity correlation of optical fields between the object path and the reference path [1]–[6]. It can restore the high-dimensional information from the low-dimensional detecting measurements by encoding the image information into the intensity fluctuations of light fields, thus providing

a new solution for high dimensional image sensing [7]–[10]. As a typical case, spectral camera based on ghost imaging via sparsity constraints (GISC spectral camera) modulates the 3D hyperspectral information into a 2D spatial intensity fluctuations of light fields, which enables capturing the 3D hyperspectral image information in a single shot [11], [12]. Combined with compressive sensing [13]–[15], it can realize compressive sensing of the information during the acquisition process with improved efficiency. However, the image reconstruction process is full of challenges. Conventional GI reconstruction algorithms, such as differential GI (DGI) [16], suffer from the low reconstruction quality in the case of low sampling rate and low signal to noise ratio. Though Compressive sensing algorithms can contribute to obtain higher reconstruction quality by utilizing prior information of the object, the time-consuming interactive process makes it difficult to reconstruct the image in real time. With recent explosive growth of artificial intelligence, deep learning (DL) has provided new opportunities and tools for computational imaging [17]–[26]. In recent years, DL has also been applied in ghost imaging and has achieved good performance [27]–[33]. Many excellent works set the detected measurements as the net input [27], [30], [33], and the sufficient sampling rate for high quality image goes down to a cheerful level. However, these works require that the measurement matrix must be the same during the training and imaging process. Zhu [28] proposes a novel dynamic decoding deep learning framework called Y-net, which introduces the statistical characteristics of the random reference measurements into the net and works well under both fixed and unfixed measurement matrix. Hu [29] and Lyu [31] have also reduced the sensibility of the measurement matrix by setting the conventional ghost imaging results as the network's input.

Compared to the 2D reconstruction in GI, introducing deep learning into the reconstruction of 3D hyperspectral information in GISC spectral camera faces the following challenges. Firstly, large-size data need to be processed due to its high dimensional property. Secondly, how to reduce the sensibility of the random reference measurements also plays an important role in the generalization ability of the network. What's more, the reconstruction quality of 3D hyperspectral information has also to be ensured. In this paper, we propose an end-to-end V-DUnet to reconstruct 3D hyperspectral images of GISC spectral camera. Owing to the encoder and decoder architecture of the Unet [34], it can effectively deal with large-

(Corresponding author: Zhentao Liu.)

Ziyan Chen, Zhentao Liu, Jianrong Wu, Jinda Lin and Zhishen Tong are with the Key Laboratory for Quantum Optics of CAS, Shanghai Institute of Optics and Fine Mechanics, Chinese Academy of Sciences, Shanghai, 201800, China and with Center of Materials Science and Optoelectronics Engineering, University of Chinese Academy of Sciences, Beijing, 100049, China.

Chenyu Hu is with Hangzhou Institute for Advanced Study, University of Chinese Academy of Sciences, Hangzhou, 310024, China.

Heng Wu is with Guangdong Provincial Key Laboratory of Cyber-Physical System, School of Automation, Guangdong University of Technology, Guangzhou, 510006, China.

Shensheng Han and Hong Yu are with the Key Laboratory for Quantum Optics of CAS, Shanghai Institute of Optics and Fine Mechanics, Chinese Academy of Sciences, Shanghai, 201800, China and with Center of Materials Science and Optoelectronics Engineering, University of Chinese Academy of Sciences, Beijing, 100049, China and with Hangzhou Institute for Advanced Study, University of Chinese Academy of Sciences, Hangzhou, 310024, China.

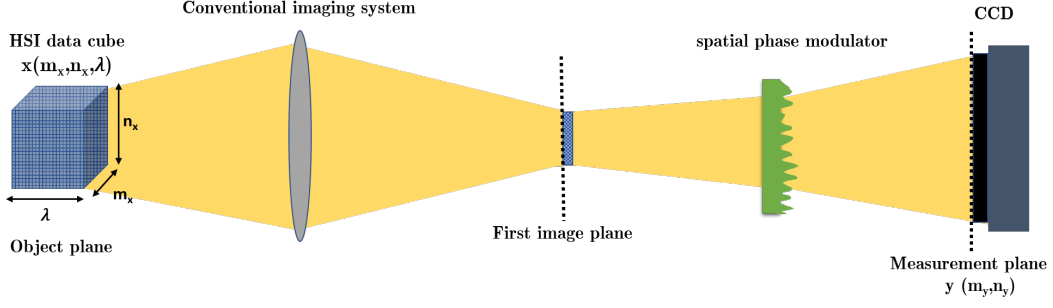


Fig. 1. The schematic of GISC spectral camera. The system is composed of three modules: (1) A front imaging module (a conventional imaging system), which projects the 3D hyperspectral data cube  $x(m_x, n_x, \lambda)$  onto the first imaging plane, (2) Modulation module (a spatial random phase modulator), which modulates the light fields in the first imaging plane, (3) Detection module (CCD), which records the speckle patterns in the measurement plane  $y(m_y, n_y)$ .

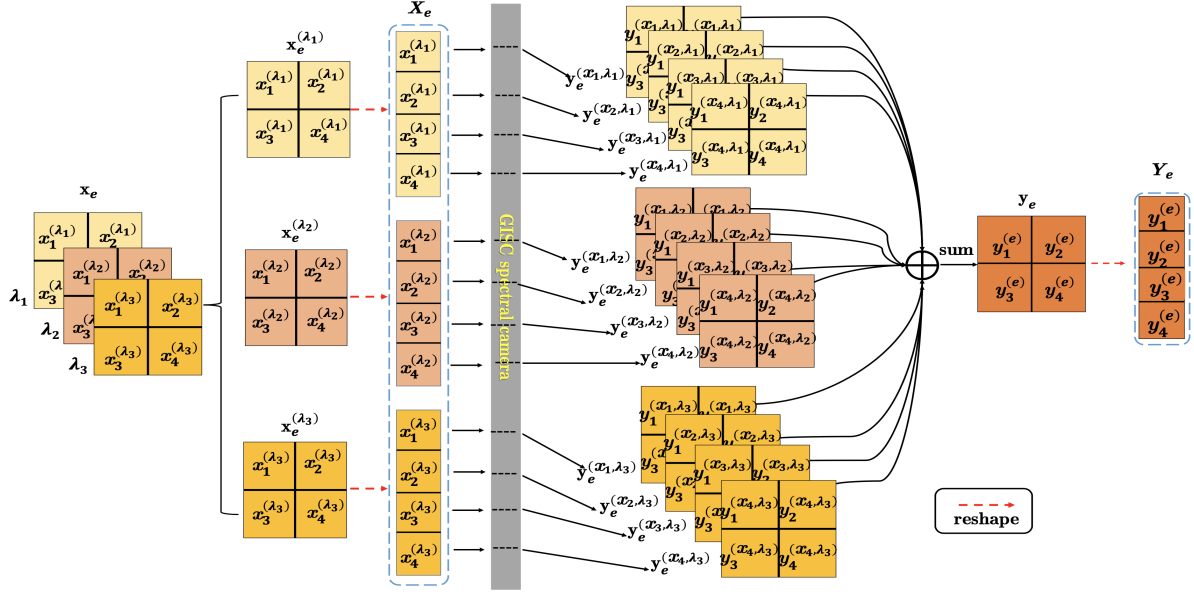


Fig. 2. An illustration of a tiny HSI data's flow in GISC spectral camera. Each pixel in data cube  $x_e$  ( $x_e$  have total 12 pixels, they are  $x_1^{(\lambda_1)}, x_2^{(\lambda_1)}, x_3^{(\lambda_1)}, x_4^{(\lambda_1)}, x_1^{(\lambda_2)}, x_2^{(\lambda_2)}, x_3^{(\lambda_2)}, x_4^{(\lambda_2)}, x_1^{(\lambda_3)}, x_2^{(\lambda_3)}, x_3^{(\lambda_3)}, x_4^{(\lambda_3)}$  respectively) contribute to a corresponding random speckle pattern ( $y_e^{(x_1, \lambda_1)}, y_e^{(x_2, \lambda_1)}, y_e^{(x_3, \lambda_1)}, y_e^{(x_4, \lambda_1)}, y_e^{(x_1, \lambda_2)}, y_e^{(x_2, \lambda_2)}, y_e^{(x_3, \lambda_2)}, y_e^{(x_4, \lambda_2)}, y_e^{(x_1, \lambda_3)}, y_e^{(x_2, \lambda_3)}, y_e^{(x_3, \lambda_3)}, y_e^{(x_4, \lambda_3)}$ , respectively) on the CCD detector plane. The detector captures the intensity  $y_e$  by integrating the total 12 random speckle patterns.

size data. And by setting both differential ghost imaging results and the detected measurements as network's input, V-DUnet has not only successfully reduced the influence caused by the uncertainty of the random reference measurements, but also improved the reconstruction quality of 3D hyperspectral images in GISC spectral camera.

## II. SYSTEM OF GISC SPECTRAL CAMERA

Fig.1 shows the schematic of GISC spectral camera. Lights from the 3D hyperspectral image (HSI)  $x(m_x, n_x, \lambda)$  are collected by a conventional imaging system in the first imaging plane and then is modulated by a spatial random phase modulator, finally, the modulated imaging speckle patterns  $y(m_y, n_y)$  are recorded by an CCD detector (each pixel in the CCD collects the intensity signal from the whole 3D hyperspectral imaging). In addition, before the imaging process, the calibrated speckle patterns are pre-determined by scanning long the spatial and spectral dimensions with

a monochromatic point source on the object plane. Thus, 3D hyperspectral images can be obtained by calculating the intensity correlation between the calibrated speckle patterns and imaging speckle patterns [12]. Meanwhile, the imaging process can be written into a matrix form as [11]

$$Y = \Phi X + \epsilon, \quad (1)$$

in which  $X \in \mathbb{R}^{M_x N_x L}$  is reshaped from the HSI data cube  $x(m_x, n_x, \lambda) \in \mathbb{R}^{M_x \times N_x \times L}$  where  $1 \leq m_x \leq M_x$ ,  $1 \leq n_x \leq N_x$  and  $1 \leq \lambda \leq L$ ,  $Y \in \mathbb{R}^{M_y N_y}$  is reshaped from the measurement image  $y(m_y, n_y) \in \mathbb{R}^{M_y \times N_y}$  where  $1 \leq m_y \leq M_y$  and  $1 \leq n_y \leq N_y$  in the CCD detector.  $\epsilon$  represents the noise of the system. The pre-determined random measurement matrix  $\Phi \in \mathbb{R}^{M_y N_y \times M_x N_x L}$  is obtained after  $M_x N_x L$  calibration measurements, each column vector in  $\Phi$  presents a calibrated speckle intensity pattern corresponding to one pixel in HSI.

In order to have an intuitive view of our GISC spectral camera sensing matrix  $\Phi$ , we choose a tiny HSI data cube

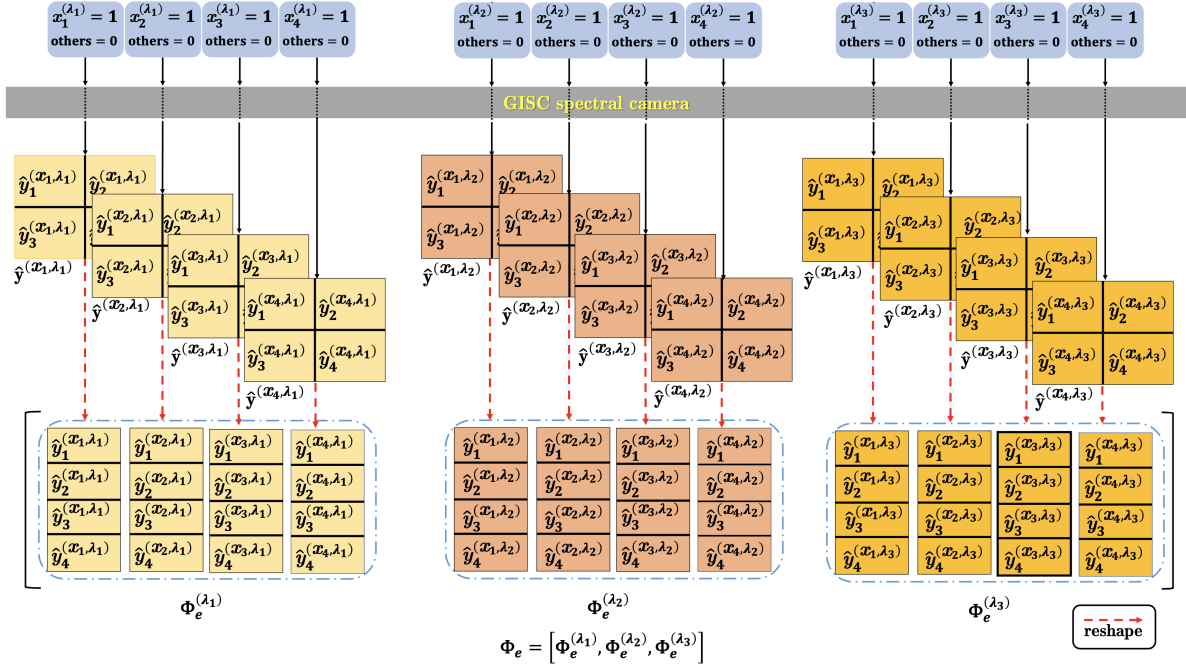


Fig. 3. Structure of the matrix  $\Phi_e$  for  $M_x = 2, N_x = 2, L = 3$  and  $M_y = 2, N_y = 2$ .

$$\Phi_e = \begin{bmatrix} \Phi_e^{(\lambda_1)} & \Phi_e^{(\lambda_2)} & \Phi_e^{(\lambda_3)} \end{bmatrix}$$

$$= \begin{bmatrix} \hat{y}_1^{(x_1, \lambda_1)} & \hat{y}_1^{(x_2, \lambda_1)} & \hat{y}_1^{(x_3, \lambda_1)} & \hat{y}_1^{(x_4, \lambda_1)} & \hat{y}_1^{(x_1, \lambda_2)} & \hat{y}_1^{(x_2, \lambda_2)} & \hat{y}_1^{(x_3, \lambda_2)} & \hat{y}_1^{(x_4, \lambda_2)} & \hat{y}_1^{(x_1, \lambda_3)} & \hat{y}_1^{(x_2, \lambda_3)} & \hat{y}_1^{(x_3, \lambda_3)} & \hat{y}_1^{(x_4, \lambda_3)} \\ \hat{y}_2^{(x_1, \lambda_1)} & \hat{y}_2^{(x_2, \lambda_1)} & \hat{y}_2^{(x_3, \lambda_1)} & \hat{y}_2^{(x_4, \lambda_1)} & \hat{y}_2^{(x_1, \lambda_2)} & \hat{y}_2^{(x_2, \lambda_2)} & \hat{y}_2^{(x_3, \lambda_2)} & \hat{y}_2^{(x_4, \lambda_2)} & \hat{y}_2^{(x_1, \lambda_3)} & \hat{y}_2^{(x_2, \lambda_3)} & \hat{y}_2^{(x_3, \lambda_3)} & \hat{y}_2^{(x_4, \lambda_3)} \\ \hat{y}_3^{(x_1, \lambda_1)} & \hat{y}_3^{(x_2, \lambda_1)} & \hat{y}_3^{(x_3, \lambda_1)} & \hat{y}_3^{(x_4, \lambda_1)} & \hat{y}_3^{(x_1, \lambda_2)} & \hat{y}_3^{(x_2, \lambda_2)} & \hat{y}_3^{(x_3, \lambda_2)} & \hat{y}_3^{(x_4, \lambda_2)} & \hat{y}_3^{(x_1, \lambda_3)} & \hat{y}_3^{(x_2, \lambda_3)} & \hat{y}_3^{(x_3, \lambda_3)} & \hat{y}_3^{(x_4, \lambda_3)} \\ \hat{y}_4^{(x_1, \lambda_1)} & \hat{y}_4^{(x_2, \lambda_1)} & \hat{y}_4^{(x_3, \lambda_1)} & \hat{y}_4^{(x_4, \lambda_1)} & \hat{y}_4^{(x_1, \lambda_2)} & \hat{y}_4^{(x_2, \lambda_2)} & \hat{y}_4^{(x_3, \lambda_2)} & \hat{y}_4^{(x_4, \lambda_2)} & \hat{y}_4^{(x_1, \lambda_3)} & \hat{y}_4^{(x_2, \lambda_3)} & \hat{y}_4^{(x_3, \lambda_3)} & \hat{y}_4^{(x_4, \lambda_3)} \end{bmatrix} \quad (3)$$

$\mathbf{x}_e \in \mathbb{R}^{2 \times 2 \times 3}$  as an example and set the  $\mathbf{y}_e \in \mathbb{R}^{2 \times 2}$  to give an illustration. What's more, we suppose the system is noise-clean for simplicity. First, the tiny HSI data's flow in GISC spectral camera is particularly illustrated in Fig.2, each pixel in HSI data cube  $\mathbf{x}_e$  produces a random speckle pattern on the CCD plane after the interaction of the conventional imaging system and the spatial random phase modulator. In our selected tiny HSI data cube  $\mathbf{x}_e$ , it has total 12 ( $M_x = 2, N_x = 2$  and  $L = 3, 2 \times 2 \times 3 = 12$ ) pixels  $x_1^{(\lambda_1)}, x_2^{(\lambda_1)}, x_3^{(\lambda_1)}, x_4^{(\lambda_1)}, x_1^{(\lambda_2)}, x_2^{(\lambda_2)}, x_3^{(\lambda_2)}, x_4^{(\lambda_2)}$ , and  $x_1^{(\lambda_3)}, x_2^{(\lambda_3)}, x_3^{(\lambda_3)}, x_4^{(\lambda_3)}$ , thus the corresponding 12 random speckle patterns are  $\mathbf{y}_e^{(x_1, \lambda_1)}, \mathbf{y}_e^{(x_2, \lambda_1)}, \mathbf{y}_e^{(x_3, \lambda_1)}, \mathbf{y}_e^{(x_4, \lambda_1)}, \mathbf{y}_e^{(x_1, \lambda_2)}, \mathbf{y}_e^{(x_2, \lambda_2)}, \mathbf{y}_e^{(x_3, \lambda_2)}, \mathbf{y}_e^{(x_4, \lambda_2)}$ , and  $\mathbf{y}_e^{(x_1, \lambda_3)}, \mathbf{y}_e^{(x_2, \lambda_3)}, \mathbf{y}_e^{(x_3, \lambda_3)}, \mathbf{y}_e^{(x_4, \lambda_3)}$ , respectively.  $\mathbf{y}_e$  is the superposition of those total 12 random speckle patterns, namely

$$\begin{aligned} \mathbf{y}_e = & \mathbf{y}_e^{(x_1, \lambda_1)} + \mathbf{y}_e^{(x_2, \lambda_1)} + \mathbf{y}_e^{(x_3, \lambda_1)} + \mathbf{y}_e^{(x_4, \lambda_1)} \\ & + \mathbf{y}_e^{(x_1, \lambda_2)} + \mathbf{y}_e^{(x_2, \lambda_2)} + \mathbf{y}_e^{(x_3, \lambda_2)} + \mathbf{y}_e^{(x_4, \lambda_2)} \\ & + \mathbf{y}_e^{(x_1, \lambda_3)} + \mathbf{y}_e^{(x_2, \lambda_3)} + \mathbf{y}_e^{(x_3, \lambda_3)} + \mathbf{y}_e^{(x_4, \lambda_3)} \end{aligned} \quad (2)$$

Second, the calibration measurement process of the sensing matrix  $\Phi_e \in \mathbb{R}^{4 \times 12}$  is displayed in Fig.3. To obtain the sensing matrix  $\Phi_e$ , one just needs to set the values of each pixel

in HSI data cube  $\mathbf{x}_e$  to 1 in sequence. As the same data flow process illustrated in Fig.2, 12 corresponding random speckle patterns  $\hat{\mathbf{y}}^{(x_1, \lambda_1)}, \hat{\mathbf{y}}^{(x_2, \lambda_1)}, \hat{\mathbf{y}}^{(x_3, \lambda_1)}, \hat{\mathbf{y}}^{(x_4, \lambda_1)}, \hat{\mathbf{y}}^{(x_1, \lambda_2)}, \hat{\mathbf{y}}^{(x_2, \lambda_2)}, \hat{\mathbf{y}}^{(x_3, \lambda_2)}, \hat{\mathbf{y}}^{(x_4, \lambda_2)}, \hat{\mathbf{y}}^{(x_1, \lambda_3)}, \hat{\mathbf{y}}^{(x_2, \lambda_3)}, \hat{\mathbf{y}}^{(x_3, \lambda_3)}, \hat{\mathbf{y}}^{(x_4, \lambda_3)}$  are generated, respectively. And the sensing matrix  $\Phi_e$  is finally obtained by reshaping all those patterns to column vectors and placing them in order, as is shown in Fig.3 and Eq.3. Finally, we let  $X_e \in \mathbb{R}^{12}$  represent the column vector reshaped from  $\mathbf{x}_e$ ,  $Y_e \in \mathbb{R}^4$  represent the column vector reshaped from  $\mathbf{y}_e$ , thus the formula between  $X_e$  and  $Y_e$  can be written as

$$Y_e = \Phi_e X_e, \quad (4)$$

in which  $Y_e = [y_1^{(e)}, y_2^{(e)}, y_3^{(e)}, y_4^{(e)}]^T$ ,  $X_e = [x_1^{(\lambda_1)}, x_2^{(\lambda_1)}, x_3^{(\lambda_1)}, x_4^{(\lambda_1)}, x_1^{(\lambda_2)}, x_2^{(\lambda_2)}, x_3^{(\lambda_2)}, x_4^{(\lambda_2)}, x_1^{(\lambda_3)}, x_2^{(\lambda_3)}, x_3^{(\lambda_3)}, x_4^{(\lambda_3)}]^T$ .

### III. THE PROPOSED FRAMEWORK

Inspired by the DAttNet [27], Unet [34], Attention Unet [35] and DenseNet [36], we propose a framework V-DUnet. As illustrated in Fig. 4, it is composed of two parts, the first part is the V part and the second part is the DUnet part. There are two inputs in V-DUnet, one is the measurement image  $\mathbf{y}$  with  $256 \times 256$  pixels recorded by the CCD, the other is the reconstructed DGI result with size  $128 \times 128 \times 15$ .

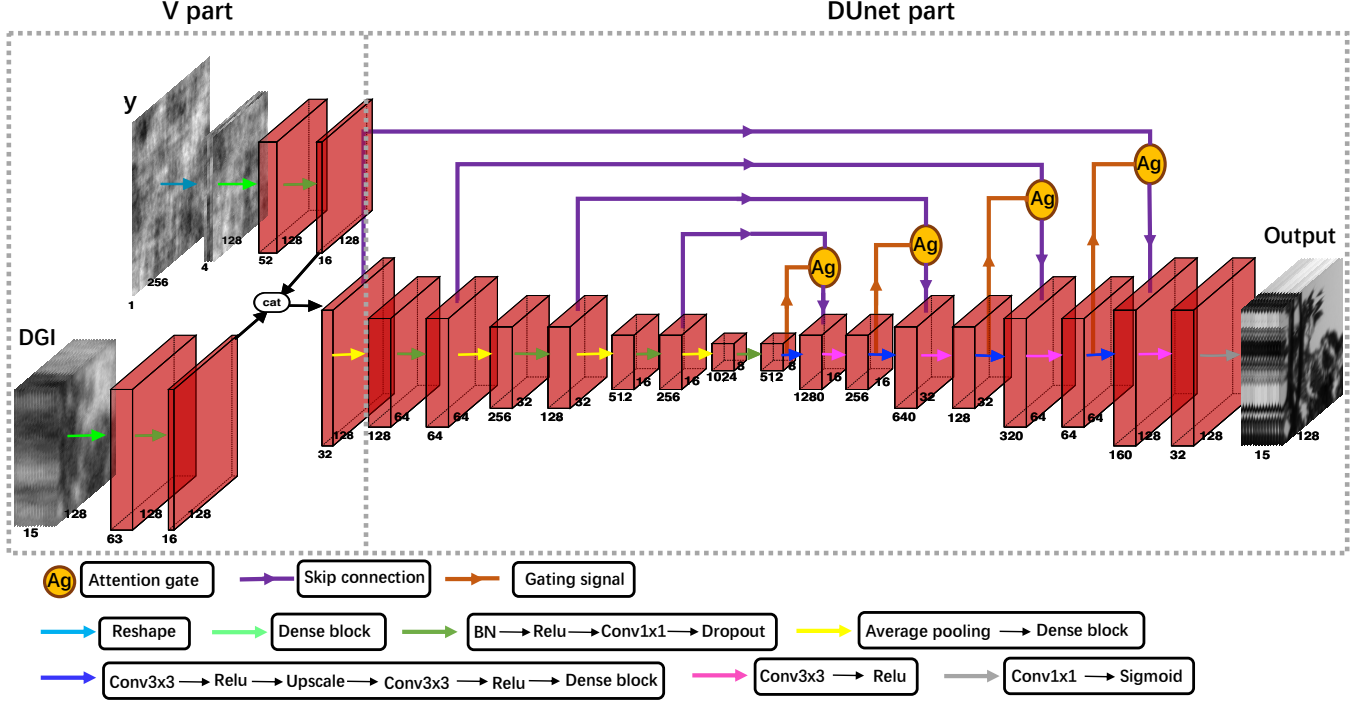


Fig. 4. The architecture of the proposed V-DUNet. BN, batch normalization; Conv  $3 \times 3$ , convolution with filter size  $3 \times 3$ ; Conv  $1 \times 1$ , convolution with filter size  $1 \times 1$ ; Dropout, dropout rate is 0.05; ReLU, rectified linear unit; Average pooling, stride (2, 2); Upscale, factor 2.

The input  $y$  is firstly reshaped into four channels with size  $128 \times 128 \times 4$ , then the reshaped result and DGI result pass through two convolutional block respectively and finally concatenated as one block (this process is corresponding to the V part of V-DUNet) and feeds into the DUnet part of V-DUNet. DUnet part is mainly designed based on DenseNet and Unet. DenseNet have four compelling advantages: (1) alleviate the vanishing-gradient problem, (2) strengthen feature propagation, (3) encourage feature reuse, and (4) substantially reduce the number of parameters [36]. The Dense block used in V-DUNet is displayed in Fig.5.

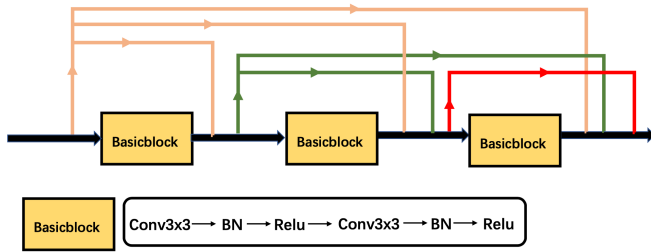


Fig. 5. The architecture of the Dense block. Each layer connects to every other layer in a feed-forward fashion.

Additionally, we apply dropout layers to prevent overfitting [37], and batch normalization (BN) layers to speed up the convergence of loss function [38]. The attention gate (AG) is also used to eliminate the irrelevant and noisy responses in Unet skip connections process, and enhance the salient

features which pass through the skip connections [34], [35]. Here we introduce the FFDNet [39] in the training process as the denoising part of V-DUNet. It can deal with a wide range of noise levels and easily remove spatially variant noise by specifying a non-uniform noise level map with a single network.

The random sensing matrix  $\Phi$  [18], [22] and the structural similarity (SSIM) [25], [40] between the ground truth and the reconstructed results are introduced into the loss function. Therefore, the loss function of our V-DUNet can be finally expressed as

$$Loss = \alpha \|X - \hat{X}\|_1 + \beta \|Y - \Phi \hat{X}\|_1 + \gamma [1 - ssim(X, \hat{X})], \quad (5)$$

here we set  $\alpha = 50$ ,  $\beta = 1$  and  $\gamma = 50$ .  $X$  represents the ground truth of the original HSI while  $\hat{X}$  is the corresponding reconstructed HSI from the net.  $ssim(X, \hat{X})$  represents the SSIM between  $X$  and  $\hat{X}$ , and it is formulated as

$$ssim(X, \hat{X}) = \frac{(2\bar{w}_X \bar{w}_{\hat{X}} + C_1)(2\sigma_{w_X w_{\hat{X}}} + C_2)}{(\bar{w}_X^2 + \bar{w}_{\hat{X}}^2 + C_1)(\sigma_{w_X}^2 + \sigma_{w_{\hat{X}}}^2 + C_2)}, \quad (6)$$

where  $w_X(w_{\hat{X}})$  represents the region of image  $X(\hat{X})$  within window  $w$  while  $\bar{w}_X(\bar{w}_{\hat{X}})$  is the mean of  $w_X(w_{\hat{X}})$ .  $\sigma_{w_X}^2(\sigma_{w_{\hat{X}}}^2)$  is the variance of  $w_X(w_{\hat{X}})$ ,  $\sigma_{w_X w_{\hat{X}}}$  represents the co-variance between  $w_X$  and  $w_{\hat{X}}$ .  $C_1$  and  $C_2$  are constants (experimentally set as  $1 \times 10^{-4}$  and  $9 \times 10^{-4}$ ), the window  $w$  is set to 11 [25].

TABLE I

THE AVERAGE EVALUATION RESULTS ON THE ICVL, CAVE AND MINHO DATASETS. 225 ICVL HSIs, 279 CAVE HSIs AND 201 MINHO HSIs ARE USED TO AVERAGE EVALUATE PSNR, SSIM AND SAM, RESPECTIVELY.

Net	Input	ICVL(225)			CAVE(279)			Minho(201)		
		PSNR	SSIM	SAM	PSNR	SSIM	SAM	PSNR	SSIM	SAM
Unet	only y	19.5750	0.4791	0.3698	16.9264	0.4189	0.4939	17.9258	0.3917	0.4207
	only DGI	25.1347	0.7557	0.1793	21.5853	0.6683	0.3068	21.5046	0.6676	0.2739
	y+DGI	25.5148	0.7720	0.1707	21.7931	0.6789	0.3034	21.6336	0.6852	0.2676
Proposed	only y	20.9977	0.6002	0.2969	18.2602	0.5476	0.4119	19.0723	0.4986	0.3671
	only DGI	25.7483	0.7635	0.1774	22.8264	0.7007	0.2919	22.8366	0.7037	0.2429
	y+DGI	<b>26.9447</b>	<b>0.7978</b>	<b>0.1565</b>	<b>23.4499</b>	<b>0.7303</b>	<b>0.2799</b>	<b>23.1362</b>	<b>0.7234</b>	<b>0.2403</b>

TABLE II

SIX DIFFERENT SCENES RECONSTRUCTED BY DIFFERENT ALGORITHMS.

Algorithm	Ours			PICHCS			TwIST			DGI		
	PSNR	SSIM	SAM	PSNR	SSIM	SAM	PSNR	SSIM	SAM	PSNR	SSIM	SAM
Scene 1	<b>30.5125</b>	<b>0.8827</b>	<b>0.1239</b>	25.4607	0.5704	0.2668	20.3763	0.2691	0.3766	14.4801	0.3471	0.5073
Scene 2	<b>30.7070</b>	<b>0.9010</b>	<b>0.0969</b>	24.8118	0.4440	0.2174	19.5310	0.1943	0.4372	14.8900	0.4787	0.2908
Scene 3	<b>32.2708</b>	<b>0.8778</b>	<b>0.1659</b>	25.4932	0.6471	0.3537	24.5597	0.4074	0.4046	14.8006	0.3795	0.4141
Scene 4	<b>31.3115</b>	<b>0.8861</b>	<b>0.1897</b>	25.9568	0.5729	0.3253	27.4102	0.6281	0.3992	12.2076	0.2326	0.5289
Scene 5	<b>32.2683</b>	<b>0.8678</b>	<b>0.1899</b>	25.3419	0.4434	0.3360	23.7993	0.3571	0.4654	16.7134	0.5047	0.3587
Scene 6	<b>31.1425</b>	<b>0.8922</b>	<b>0.1437</b>	21.3948	0.4542	0.3170	20.5054	0.2671	0.5294	14.4138	0.4230	0.4168
Average	<b>31.3688</b>	<b>0.8846</b>	<b>0.1523</b>	24.7432	0.5220	0.2961	22.6970	0.3538	0.4354	14.6509	0.3943	0.4194

TABLE III

ANTI-NOISE PERFORMANCE COMPARISONS ON THE ICVL, CAVE AND MINHO DATASETS FOR THE CASES WITH SNR 30 dB AND SNR 10 dB. 225 ICVL HSIs, 279 CAVE HSIs AND 201 MINHO HSIs ARE USED TO AVERAGE EVALUATE PSNR, SSIM AND SAM, RESPECTIVELY.

SNR	ICVL(225)			CAVE(279)			Minho(201)		
	PSNR	SSIM	SAM	PSNR	SSIM	SAM	PSNR	SSIM	SAM
30 dB	26.9447	0.7978	0.1565	23.4499	0.7303	0.2799	23.1362	0.7234	0.2403
10 dB	26.8888	0.7890	0.1526	23.2716	0.7157	0.2814	22.5408	0.7058	0.2421

#### IV. SIMULATION RESULTS

Three public HSI datasets are used to evaluate our method, including the ICVL dataset [41], CAVE dataset [42] and the Minho dataset [43]. The ICVL dataset consists of 201 HSIs ( $1024 \times 1392 \times 31$ ) and the CAVE dataset consists of 32 images ( $512 \times 512 \times 31$ ), the spectral bands of both the ICVL and CAVE datasets are ranged from 400 nm to 700 nm with 10 nm intervals. The Minho dataset consists of 30 HSIs ( $820 \times 820 \times 31$ ), the wavelength range of 410 nm–720 nm was sampled at 10 nm intervals. We choose 15 channels with spectral range from 560 nm to 700 nm in those datasets.

To eliminate the overfitting effect, we manually exclude 91 HSIs with similar background or contents and selected 110 HSIs in ICVL dataset. Then we randomly select 101 HSIs in the subsets for training and thus use the rest 9 HSIs for testing. To formulate the training and validation datasets, HSI patches

with the size of  $128 \times 128 \times 15$  are uniformly extracted with the stride of 128 from the above 101 HSIs in ICVL dataset. We randomly select 90% patches for training and 10% patches for validation. As for the CAVE and Minho dataset, none of them has been included in the training dataset, they are only used for testing. We randomly crop 225 HSI patches from the rest 9 HSIs in ICVL dataset, 279 HSI patches from the CAVE dataset and 201 HSI patches from the Minho dataset for testing. All the models are only trained on ICVL dataset and another input  $y$  for training is obtained by Eq.1, where the detected Signal to Noise Ratio (SNR) is 30 dB and  $\Phi$  is obtained by the calibration of GISC spectral camera.

Three quantitative image quality metrics, including peak signal-to-noise ratio (PSNR), SSIM and spectral angle mapping (SAM) [44], are used to evaluate the performance of all methods. Larger PSNR, SSIM and the smaller SAM values

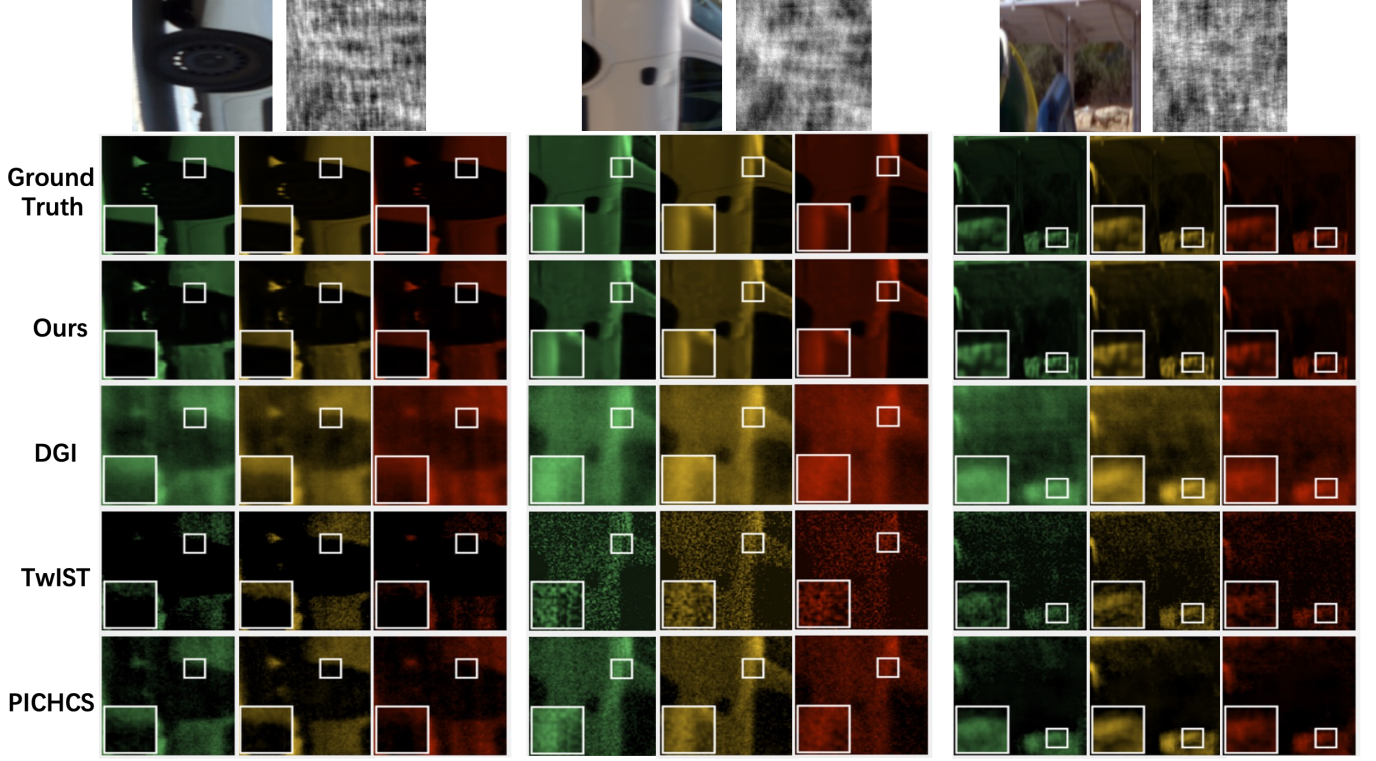


Fig. 6. Exemplar reconstructed images by 4 algorithms for three scenes (from left to right: Scene 1, Scene 2, Scene 3). The upper figures are the synthetic RGB and the image  $y$  respectively. Three ( $560\text{ nm}$ ,  $630\text{ nm}$  and  $700\text{ nm}$ ) out of 15 spectral channels are shown to compare with the ground truth.

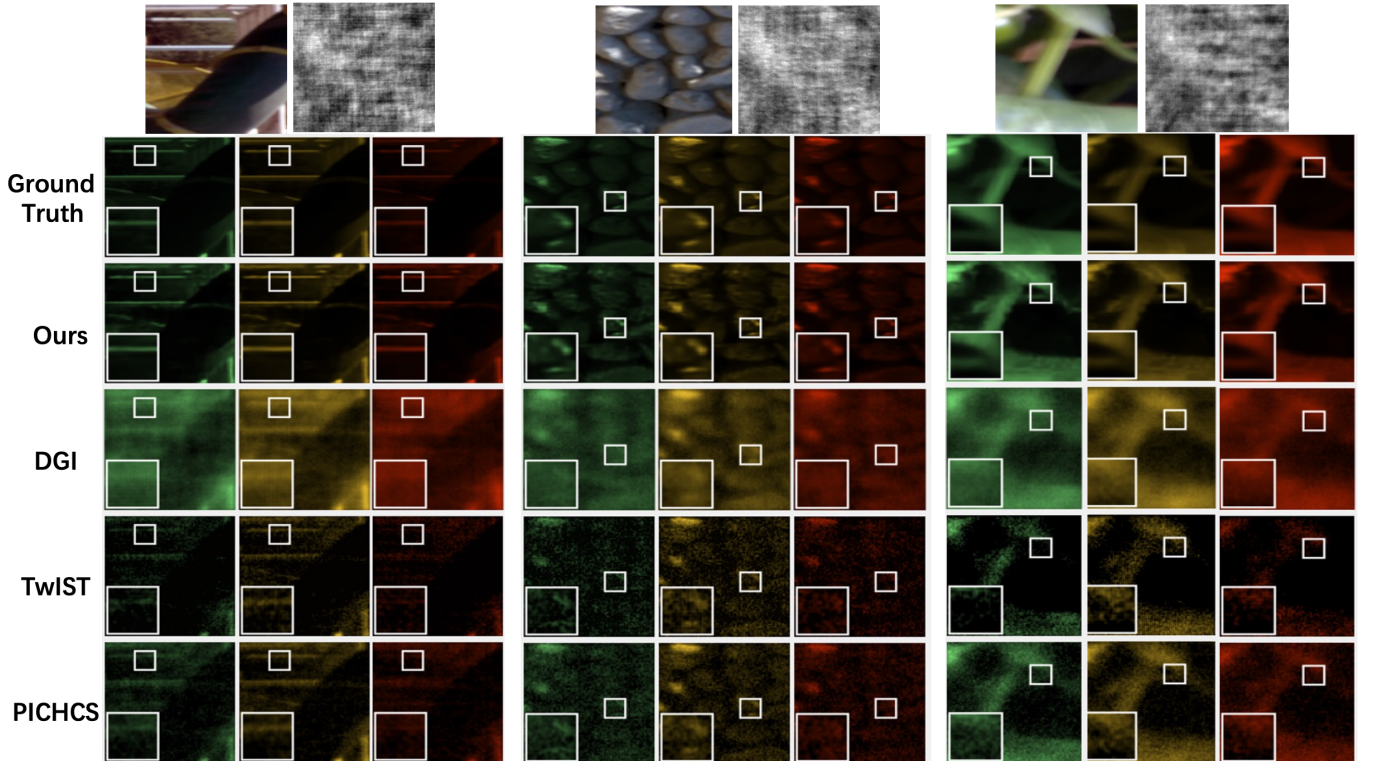


Fig. 7. Exemplar reconstructed images by 4 algorithms for three scenes (from left to right: Scene 4, Scene 5, Scene 6). The upper figures are the synthetic RGB and the image  $y$  respectively. Three ( $560\text{ nm}$ ,  $630\text{ nm}$  and  $700\text{ nm}$ ) out of 15 spectral channels are shown to compare with the ground truth.

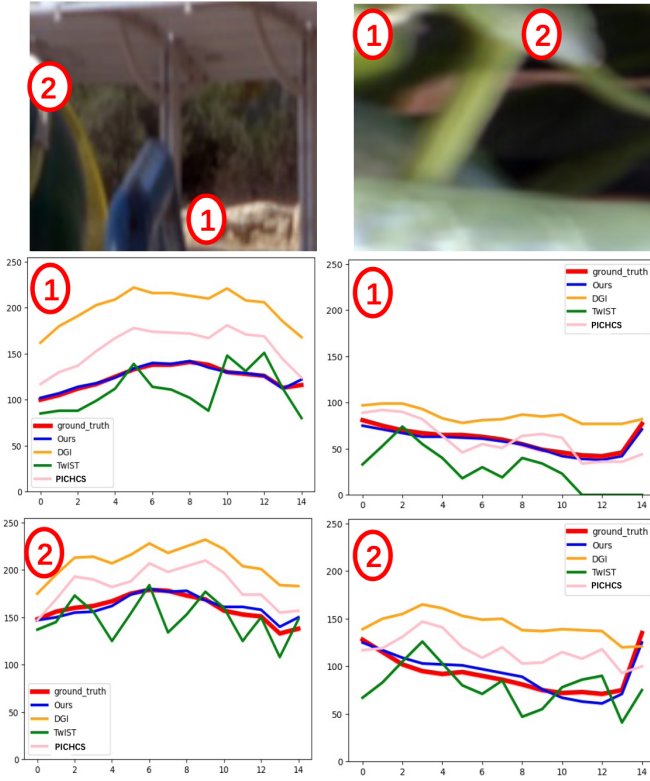


Fig. 8. Spectral curves of the Scene 3 and Scene 6.

suggest better reconstruction performance, and vice versa.

The effects of different inputs of the V part in the net have also taken into account during the net design process, see TABLE I. It is obvious that when only  $y$  is used as input, the net reconstruction result is unsatisfactory for neither Unet nor DUNet. When the net inputs are DGI and  $y$ , the average improvement in PSNR of reconstructed result has greatly achieved about 6 dB compared with the case when the net input is only  $y$ , and about 1 dB compared with the case when the net input is only DGI. As shown in TABLE I, compared with the case when only basic Unet is used in the second part of the net, DUNet which is mainly designed by Dense block and Unet obtains better reconstruction performance.

To verify the performance of our proposed method, we compare it with several representative reconstruction methods including DGI, TwiST [45], and PICHCS [46]. We have made great effort to achieve the best results of all those competitive methods. To visualize the experimental results for all methods, several representative reconstructed image for 6 scenes on ICVL dataset are shown in Fig. 6 and Fig. 7. The PSNR, SSIM and SAM using V-DUNet and other three algorithms are listed in TABLE II. Fig. 6 and Fig. 7 shows that our V-DUNet has achieved visually pleasant results with more details of the images compared with other three methods, which is consistent with the numerical evaluation metrics listed in TABLE II. The spectral curves of the reconstruction and ground truth have been plotted in Fig. 8. It can be seen that spectral curves of our method are more close to the ground truth which further demonstrates that V-DUNet can extract more spectral

information compared with other methods. TABLE III shows the noise tolerance performance of V-DUNet, where the cases with SNR 30 dB and 10 dB are verified with the same training weights. We can see that when the SNR decreases to 10 dB from 30 dB, the reconstructed results just slightly degenerated, which demonstrates that our method is robust to the noise.

## V. CONCLUSION

This paper aims to improve the image reconstruction quality and real-time performance in GISC spectral camera. Inspired by the recent advances of deep learning, we proposed an end-to-end V-DUNet to obtain the 3D hyperspectral images in GISC spectral camera. It can quickly reconstruct high-quality 3D hyperspectral images by integrating DenseNet into the Unet framework and setting both differential ghost imaging results and the detected measurements as the network's input. As observed in TABLE III, V-DUNet is also robust to the noise. In view of the well performance of the network, it is expected to be applied into super-resolution imaging via discernibility in high-dimensional light-field space [47] and other high-dimensional imaging system [48], [49].

## REFERENCES

- [1] D. V. Strelakov, A. V. Sergienko, D. N. Klyshko, and Y. H. Shih, "Observation of two-photon "ghost" interference and diffraction," vol. 74, no. 18, pp. 3600–3603, may 1995.
- [2] J. Cheng and S. Han, "Incoherent coincidence imaging and its applicability in x-ray diffraction," vol. 92, no. 9, p. 093903, mar 2004.
- [3] A. Gatti, E. Brambilla, M. Bache, and L. A. Lugiato, "Ghost imaging with thermal light: Comparing entanglement and ClassicalCorrelation," vol. 93, no. 9, p. 093602, aug 2004.
- [4] M. I. Kolobov, *Quantum Imaging*, 2007.
- [5] Y. Shih, "The physics of ghost imaging." OSA, 2008.
- [6] J. H. Shapiro and R. W. Boyd, "The physics of ghost imaging," vol. 11, no. 4, pp. 949–993, jan 2012.
- [7] M. F. Duarte, M. A. Davenport, D. Takhar, J. N. Laska, T. Sun, K. F. Kelly, and R. G. Baraniuk, "Single-pixel imaging via compressive sampling," vol. 25, no. 2, pp. 83–91, mar 2008.
- [8] C. Zhao, W. Gong, M. Chen, E. Li, H. Wang, W. Xu, and S. Han, "Ghost imaging lidar via sparsity constraints," vol. 101, no. 14, p. 141123, oct 2012.
- [9] N. D. Hardy and J. H. Shapiro, "Computational ghost imaging versus imaging laser radar for three-dimensional imaging," vol. 87, no. 2, p. 023820, feb 2013.
- [10] B. Sun, M. P. Edgar, R. Bowman, L. E. Vittert, S. Welsh, A. Bowman, and M. J. Padgett, "3d computational imaging with single-pixel detectors," vol. 340, no. 6134, pp. 844–847, may 2013.
- [11] S. Han, H. Yu, X. Shen, H. Liu, W. Gong, and Z. Liu, "A review of ghost imaging via sparsity constraints," vol. 8, no. 8, p. 1379, aug 2018.
- [12] Z. Liu, S. Tan, J. Wu, E. Li, X. Shen, and S. Han, "Spectral camera based on ghost imaging via sparsity constraints," vol. 6, no. 1, may 2016.
- [13] D. Donoho, "Compressed sensing," vol. 52, no. 4, pp. 1289–1306, apr 2006.
- [14] E. Candes, J. Romberg, and T. Tao, "Robust uncertainty principles: exact signal reconstruction from highly incomplete frequency information," vol. 52, no. 2, pp. 489–509, feb 2006.
- [15] Y. C. Eldar and G. Kutyniok, Eds., *Compressed Sensing*. Cambridge University Press, 2009.
- [16] F. Ferri, D. Magatti, L. A. Lugiato, and A. Gatti, "Differential ghost imaging," vol. 104, no. 25, p. 253603, jun 2010.
- [17] G. Barbastathis, "On the use of deep learning for computational imaging," K. Dholakia and G. C. Spalding, Eds. SPIE, sep 2020.
- [18] F. Wang, Y. Bian, H. Wang, M. Lyu, G. Pedrini, W. Osten, G. Barbastathis, and G. Situ, "Phase imaging with an untrained neural network," vol. 9, no. 1, may 2020.
- [19] X. Yuan, D. J. Brady, and A. K. Katsaggelos, "Snapshot compressive imaging: Theory, algorithms, and applications," vol. 38, no. 2, pp. 65–88, mar 2021.

- [20] X. Miao, X. Yuan, Y. Pu, and V. Athitsos, "lambda-net: Reconstruct hyperspectral images from a snapshot measurement." IEEE, oct 2019.
- [21] L. Wang, T. Zhang, Y. Fu, and H. Huang, "HyperReconNet: Joint coded aperture optimization and image reconstruction for compressive hyperspectral imaging," vol. 28, no. 5, pp. 2257–2270, may 2019.
- [22] T. Zhang, Y. Fu, L. Wang, and H. Huang, "Hyperspectral image reconstruction using deep external and internal learning." IEEE, oct 2019.
- [23] L. Wang, C. Sun, Y. Fu, M. H. Kim, and H. Huang, "Hyperspectral image reconstruction using a deep spatial-spectral prior." IEEE, jun 2019.
- [24] W. Zhang, H. Song, X. He, L. Huang, X. Zhang, J. Zheng, W. Shen, X. Hao, and X. Liu, "Deeply learned broadband encoding stochastic hyperspectral imaging," vol. 10, no. 1, may 2021.
- [25] J. Zhang, Y. Sun, J. Chen, D. Yang, and R. Liang, "Deep-learning-based hyperspectral recovery from a single RGB image," vol. 45, no. 20, p. 5676, oct 2020.
- [26] N. Sharma and M. Hefeeda, "Hyperspectral reconstruction from RGB images for vein visualization." ACM, may 2020.
- [27] H. Wu, R. Wang, G. Zhao, H. Xiao, D. Wang, J. Liang, X. Tian, L. Cheng, and X. Zhang, "Sub-nyquist computational ghost imaging with deep learning," vol. 28, no. 3, p. 3846, jan 2020.
- [28] R. Zhu, H. Yu, Z. Tan, R. Lu, S. Han, Z. Huang, and J. Wang, "Ghost imaging based on y-net: a dynamic coding and decoding approach," vol. 28, no. 12, p. 17556, may 2020.
- [29] H.-K. Hu, S. Sun, H.-Z. Lin, L. Jiang, and W.-T. Liu, "Denoising ghost imaging under a small sampling rate via deep learning for tracking and imaging moving objects," vol. 28, no. 25, p. 37284, nov 2020.
- [30] F. Wang, H. Wang, H. Wang, G. Li, and G. Situ, "Learning from simulation: An end-to-end deep-learning approach for computational ghost imaging," vol. 27, no. 18, p. 25560, aug 2019.
- [31] M. Lyu, W. Wang, H. Wang, H. Wang, G. Li, N. Chen, and G. Situ, "Deep-learning-based ghost imaging," vol. 7, no. 1, dec 2017.
- [32] Y. He, G. Wang, G. Dong, S. Zhu, H. Chen, A. Zhang, and Z. Xu, "Ghost imaging based on deep learning," vol. 8, no. 1, apr 2018.
- [33] F. Li, M. Zhao, Z. Tian, F. Willomitzer, and O. Cossairt, "Compressive ghost imaging through scattering media with deep learning," vol. 28, no. 12, p. 17395, may 2020.
- [34] O. Ronneberger, P. Fischer, and T. Brox, "U-net: Convolutional networks for biomedical image segmentation." Springer International Publishing, 2015, pp. 234–241.
- [35] O. Oktay, J. Schlemper, L. L. Folgoc, M. Lee, M. Heinrich, K. Misawa, K. Mori, S. McDonagh, N. Y. Hammerla, B. Kainz, B. Glocker, and D. Rueckert, "Attention u-net: Learning where to look for the pancreas," Apr. 2018.
- [36] G. Huang, Z. Liu, L. V. D. Maaten, and K. Q. Weinberger, "Densely connected convolutional networks." IEEE, jul 2017.
- [37] A. Krizhevsky, I. Sutskever, and G. E. Hinton, "ImageNet classification with deep convolutional neural networks," vol. 60, no. 6, pp. 84–90, may 2017.
- [38] S. Ioffe and C. Szegedy, "Batch normalization: Accelerating deep network training by reducing internal covariate shift," Feb. 2015.
- [39] K. Zhang, W. Zuo, and L. Zhang, "FFDNet: Toward a fast and flexible solution for CNN-based image denoising," vol. 27, no. 9, pp. 4608–4622, sep 2018.
- [40] Z. Wang, A. Bovik, H. Sheikh, and E. Simoncelli, "Image quality assessment: From error visibility to structural similarity," vol. 13, no. 4, pp. 600–612, apr 2004.
- [41] B. Arad and O. Ben-Shahar, "Sparse recovery of hyperspectral signal from natural RGB images." Springer International Publishing, 2016, pp. 19–34.
- [42] F. Yasuma, T. Mitsunaga, D. Iso, and S. K. Nayar, "Generalized assorted pixel camera: Postcapture control of resolution, dynamic range, and spectrum," vol. 19, no. 9, pp. 2241–2253, sep 2010.
- [43] S. M. C. Nascimento, F. P. Ferreira, and D. H. Foster, "Statistics of spatial cone-excitation ratios in natural scenes," vol. 19, no. 8, p. 1484, aug 2002.
- [44] F. Kruse, A. Lefkoff, J. Boardman, K. Heidebrecht, A. Shapiro, P. Barloon, and A. Goetz, "The spectral image processing system (SIPS)—interactive visualization and analysis of imaging spectrometer data," vol. 44, no. 2-3, pp. 145–163, may 1993.
- [45] J. Bioucas-Dias and M. Figueiredo, "A new TwIST: Two-step iterative shrinkage/thresholding algorithms for image restoration," vol. 16, no. 12, pp. 2992–3004, dec 2007.
- [46] S. Tan, Z. Liu, E. Li, and S. Han, "Hyperspectral compressed sensing based on prior images constrained," vol. 35, no. 8, p. 0811003, 2015.
- [47] Z. Tong, Z. Liu, J. Wang, X. Shen, and S. Han, "Breaking rayleigh's criterion via discernibility in high-dimensional light-field space with snapshot ghost imaging," Mar. 2020.
- [48] C. Chu, S. Liu, Z. Liu, C. Hu, Y. Zhao, and S. Han, "Spectral polarization camera based on ghost imaging via sparsity constraints," vol. 60, no. 16, p. 4632, may 2021.
- [49] G. R. Arce, D. J. Brady, L. Carin, H. Arguello, and D. S. Kittle, "Compressive coded aperture spectral imaging: An introduction," vol. 31, no. 1, pp. 105–115, jan 2014.